Comparison of the RHT Concrete Material Model in LS-DYNA and ANSYS AUTODYN

Christian Heckötter[1], Jürgen Sievers[1]

[1]Gesellschaft für Anlagen- und Reaktorsicherheit (GRS) gGmbH, Department of Barrier Effectiveness,
Schwertnergasse 1, 50667 Cologne, Germany

Abstract

The goal of this paper is to compare the implementations of the RHT concrete model developed by Riedel, Hiermaier and Thoma in the commercial hydrocodes ANSYS AUTODYN and LS-DYNA for different stress conditions. The considered stress conditions include hydrostatic compaction related to the Mie-Grüneisen equation of state in conjunction with a p-α model, uniaxial tension, uniaxial compression and tri-axial compression. Parameters of the failure surface and residual strength surface were fitted to data of several tri-axial compression tests. Major differences are observed regarding the behaviour under uniaxial tension. It is pointed out that the current model implementations do not consider fracture energy. Hence, the simulation results depend inherently on mesh size in cases where tensile properties are relevant.

Furthermore, comparative validation studies based on impact tests dealing with punching failure of reinforced concrete slabs subjected to hard missile impact have been performed. The sensitivity of the ballistic limit velocity as well as residual missile velocities on model parameters is discussed.

The work of GRS was carried out in the framework of the German reactor safety research program sponsored by the German Federal Ministry of Economic Affairs and Energy (BMWi).

1 Introduction

The RHT concrete model developed by Riedel, Hiermaier and Thoma [1], [2] was originally implemented in the commercial hydrocode ANSYS AUTODYN [3]. Later it has been added as `*MAT_272` [4] to the material library of LS-DYNA [5].

The present paper compares the behaviour of the RHT model in the implementations for certain quasi-static stress states. Section 2 is dealing with hydrostatic compression according to the p-α equation of state (EOS) [6]. Uniaxial tension and issues of mesh size dependency are addressed in section 3. Section 4 is dealing with unconfined uniaxial compression and tri-axial compression.

In principle a user of the RHT concrete model is confronted with the challenge to enter over 30 input parameters. In this context a parameter set called CONC-35 provided by Riedel [1] for a concrete with a compressive strength of 35 MPa is a very useful starting point. In this paper some parameters are fitted to results of tri-axial compressive tests provided to the participants of the activity IRIS ("Improving the Robustness Assessment Methodologies for Structures Impacted by Missiles") hosted by the NEA (Nuclear Energy Agency) of OECD. Details about the IRIS benchmark are given e.g. in references [7], [8] and [9].

Results from comparative analyses on selected impact tests dealing with punching failure and perforation of reinforced concrete slabs subjected to hard missile impact are presented in section 5. These tests were carried out at the Technical Research Centre of Finland (VTT). Some of these tests were addressed in the IRIS activity. Results from further comparative studies include impact tests dealing with flexural failure of reinforced concrete slabs subjected to soft missile impact and tests dealing with reinforced concrete under contact detonation and blast loading. Numerical investigations based on these tests are documented in [10].

A comparative listing of the model input parameters is provided in an annex in section 7.

2 Hydrostatic compression

Regarding the hydrostatic behaviour of porous concrete the RHT model utilizes the so-called p-*α* equation of state (EOS) introduced by Herrmann [6]. In this context, the porosity α is defined by equation (1) as ratio of the specific volumes of porous material $v = 1/\rho$ and matrix material $v_{solid} = 1/\rho_{solid}$. In AUTODYN the user is prompted to enter initial solid density $\rho_{\mathrm{solid},0}$ and porous density $\rho_{\mathrm{porous},0}$ at zero pressure, while the initial porosity α_{e} is entered in LS-DYNA. In the CONC-35 parameter set the values of $\rho_{solid,0}$ = 2.75 g/cm^3 and $\rho_{porous,0}$ = 2.341 g/cm^3 yield α_{e} = 1.1884.

$$\alpha = \frac{v}{v_{solid}} = \frac{\rho_{solid}}{\rho} \tag{1}$$

In general, the compression μ is defined by equation (2) with current density ρ and density ρ_0 at zero pressure.

$$\mu = \frac{\rho}{\rho_0} - 1 \tag{2}$$

Commonly an EOS is a function *f* according to equation (3) that relates hydrostatic pressure p, specific volume *v* and internal energy *e*.

$$p = f(v,e) \tag{3}$$

One basic assumption of the p-*α* EOS is that the internal energies of matrix material and porous material are identical. It is assumed that a given EOS in form of equation (2) for the matrix material can be applied to the porous material according to equation (4). The first form is given by Herrmann [6]. Carrol and Holt [11] give the latter form in equation (4) which is utilized by the RHT model.

$$p = f\left(\frac{v}{\alpha}, e\right) \quad \text{or} \quad p = \frac{1}{\alpha} \cdot f\left(\frac{v}{a}, e\right) \tag{4}$$

The RHT model employs the polynomial EOS for the matrix material given in equation (5).

$$p = \begin{cases} A_1 \cdot \mu + A_2 \cdot \mu^2 + A_3 \cdot \mu^3 + (B_0 + B_1 \cdot \mu) \cdot \rho_0 \cdot e & \text{if} \quad \mu \geq 0 \\ T_1 \cdot \mu + T_2 \cdot \mu^2 + B_0 \cdot \rho_0 \cdot e & \text{if} \quad \mu < 0 \end{cases} \tag{5}$$

Alternatively, in the LS-DYNA implementation equation (6) may be used if $B_0 = 0$ is selected. This form contains the Grüneisen-parameter *Γ*. In case of $B_0 = B_1 = \Gamma = 0$ equation (5) and (6) are identical for $\mu \geq 0$.

$$p = \Gamma \cdot \rho_0 \cdot e + \left[A_1 \cdot \mu + A_2 \cdot \mu^2 + A_3 \cdot \mu^3\right] \cdot \left[1 - \frac{1}{2} \cdot \Gamma \cdot \mu\right] \tag{6}$$

Schematically, the relationship of porosity and hydrostatic pressure is illustrated in Fig. 1. Initially, the compaction is elastic in the range between α_e and α_p. In this range the initial porosity is fully recovered after unloading. Plastic pore collapse occurs, when initial compaction pressure p_e is exceeded. This value is chosen based on the compressive strength as 2/3*f_c [1]. After unloading according to equation (4) a certain pore compaction remains. At the solid compaction pressure p_s the material is fully compacted and no pores are left. This corresponds to a porosity of $\alpha = 1$. This occurs at p_s = 6 GPa in the CONC-35 parameter set. At this pressure the loading curve exhibits an infinite slope.

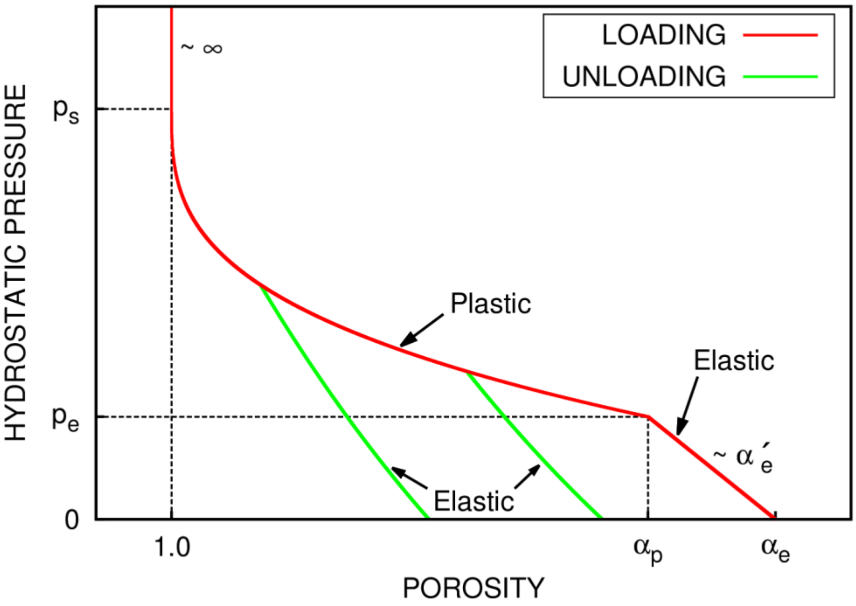

Fig. 1: Schematic compaction behaviour of a porous material due to hydrostatic pressure in the p-α model by Herrmann [6] (not to scale)

The calculation of the porosity requires an additional equation. According to Herrmann [6] equation (7) is capable to cover the compaction process described above. This equation is employed in the AUTODYN implementation of the RHT model since version 16.0.

$$\alpha(p) = 1 + (\alpha_p - 1) \cdot \left(\frac{p_{solid} - p}{p_{solid} - p_{el}} \right)^n \tag{7}$$

In the LS-DYNA implementation the time dependent equation (8) is used for the calculation of the porosity. This form corresponds to the EOS available under the keyword **`*EOS_MIE_GRUNEISEN`**.

$$\alpha(t) = \max\left(1, \min\left\{ \alpha_e, \min_{s \le t} \left[1 + (\alpha_e - 1) \cdot \left(\frac{p_{solid} - p(s)}{p_{solid} - p_{el}} \right)^n \right] \right\} \right) \tag{8}$$

Basically, equation (8) deviates regarding two features from equation (7). First of all, the history variable α is monotonically increasing with time. That is, recovery of porosity after unloading as well as initial elastic compaction behaviour cannot be addressed by **`*EOS_MIE_GRUNEISEN`**. Further, the algebraic form of the interior brackets deviates, since α_e instead of α_p is used. The porosity at initial compaction pressure can be calculated by equation (9).

$$\alpha_p = \alpha_e + p_e \cdot \alpha'_e \tag{9}$$

According to Herrmann [6] the slope in the elastic range is given by (10), with bulk modulus K_0 of concrete, longitudinal sound-speed of porous concrete c_e (at $p = 0$ and ρ_{porous}) and longitudinal sound-speed of the matrix material c_0 (at $p = 0$ and $\rho_{solid,0}$).

$$\alpha'_e = \frac{\alpha_e}{K_0} - \frac{\alpha_e^2}{K_0} \cdot \frac{c_0^2}{c_e^2} \tag{10}$$

In the CONC-35 parameter set $K_0 = 19.97$ GPa, $c_e = 2920$ m/s and $c_0 = 3581$ m/s yield $\alpha_p \approx 1.1873$. Sound-speeds, densities and bulk moduli are related by equations (11) and (12).

$$c_e^2 \cdot \rho_{porous0} = K_0 \tag{11}$$

$$c_0^2 \cdot \rho_{solid,0} = A_1 \tag{12}$$

© 2017 Copyright by DYNAmore GmbH

In the AUTODYN implementation A_1, $\rho_{solid,0}$ and c_e are direct input parameters. Input parameters related to K_0 or c_e are missing in the LS-DYNA implementation. Instead, the LS-DYNA implementation uses $A_1 = K_0$, which is supposed to be in general an unrealistic choice. The differences among the implementations are illustrated by results of a single-element simulation shown in Fig. 2. In order to eliminate effects of internal energy, $B_1 = B_0 = \Gamma = 0$ was chosen. The AUTODYN (version 16.0 and higher) results regarding pressure-porosity and pressure-density relationships reproduce the expected model-behaviour as it is described by Riedel [1]. As mentioned above, equation (8) used by LS-DYNA is not capable to consider elastic pore deformation. Further, changes in porosity during unloading and reloading after initial pore collapse has occurred are not considered. The difference in the algebraic form yields a different porosity value at the beginning of pore collapse. It is apparent from the pressure-density relationship that the bulk moduli in the elastic region deviate. Further differences are visible in the unloading und reloading behaviour after pore collapse. Due to $K_0 < A_1$ in the CONC-35 parameter set, the LS-DYNA response is somewhat stiffer. In cases where the propagation of longitudinal waves is a relevant issue, the mentioned differences between the two implementations may become important.

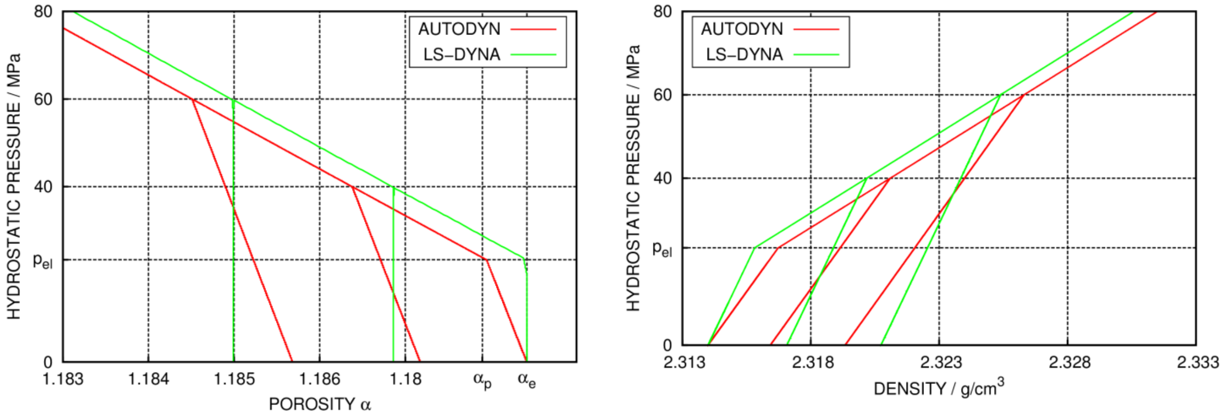

Fig. 2: Code comparison of the compaction behaviour due to hydrostatic pressure including unloading and reloading behaviour

3 Uniaxial tension

Material damage is initiated, if further plastic damage occurs after the initial failure surface was reached. The model calculates a damage parameter D according to equation (13) by accumulation of increments of effective plastic strain. For a damage of $D = 1$ the residual strength surface is reached.

$$0 \le D = \sum_{\Delta} \frac{\Delta\varepsilon_{pl,eff}}{\varepsilon_f(p)} \le 1 \tag{13}$$

The failure strain is calculated by equation (14) with the input parameters D_1, D_2, f_t^* and $\varepsilon_{f,min}$. The superscript * denotes that quantities are related to the compressive strength f_c. The maximum strain to failure $\varepsilon_{f,min}$ of the CONC-35 parameter set is based on tests dealing with cyclic compressive loading (see [1]).

$$\varepsilon_f(p) = D_1 \cdot \left(p^* - f_t^*\right)^{D_2} \ge \varepsilon_{f,\min} \tag{14}$$

The maximum obtainable tensile pressure is limited according to equation (15) by the hydrodynamic tensile limit P_{min} and the EOS. Since P_{min} is derived by the tensile strength f_t^*, no further input is required.

$$p = \max\left(\left(1-D\right)\cdot P_{\min}, \frac{1}{\alpha}\cdot f\left(\frac{v}{\alpha}, e\right)\right) \tag{15}$$

One shortcoming of the failure model is that discretisation length or fracture energy is not included. Therefore, results regarding tensile failure are inherently dependent from the mesh size. An interesting extension of the failure model is presented by Leppänen [12]. It includes the integration of an additional Rankine failure surface for tensile cracking and a bi-linear softening law. Fig. 3 compares results for single element simulations. Up to a stress of *tensrat*f$_t$* the behaviour is elastic. After reaching the uniaxial tensile strength of $f_t = 3.5$ MPa, tensile softening and damage accumulation occur. In this displacement-controlled single element simulation the tensile stress vanishes only at the maximum strain to failure $\varepsilon_{f,min}$ of about 1%. It is remarkable that the softening branch is not perfectly straight in the AUTODYN simulation. In LS-DYNA the input parameter PTF may be used to control the direction of plastic flow in tension. As reported in [4], a value of PTF = 1.0 may be used to avoid noise in tension. Some noise is visible in the calculation with PTF = 0.001. Regarding the relationship of damage parameter and effective plastic strain, the models give identical results. However, the parameter PTF has some effect on the values of maximum principal strains.

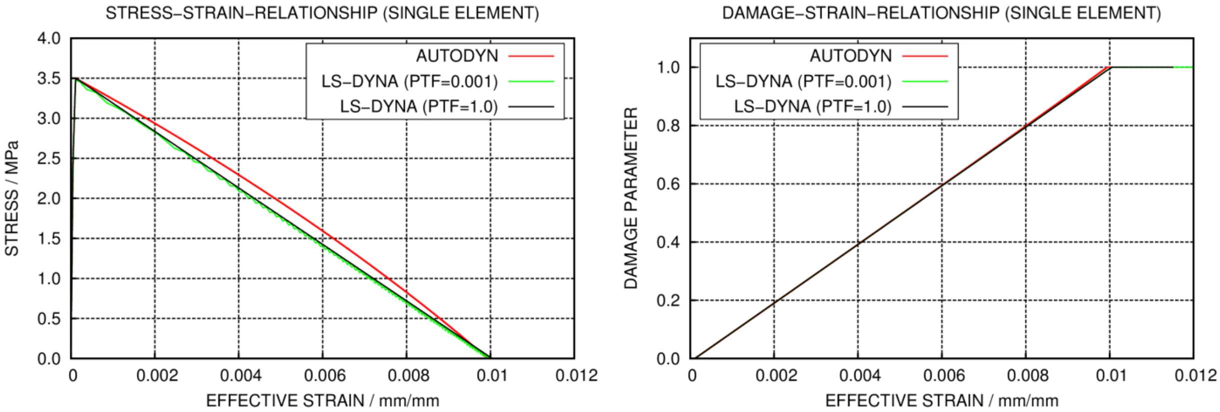

Fig. 3: Code comparison of tensile softening behaviour and damage parameter evolution in single-element

The effect of mesh size is illustrated by simulations of a hypothetical displacement-controlled tensile test with a notched specimen. Fig. 4 shows contours of the damage parameter obtained in a parameter study regarding mesh size. It is apparent that in the LS-DYNA simulations the damage occurs mainly in the plane of the notch, while unrealistic crack patterns with cracks outside the plane of the notch develop in the AUTODYN simulations. As a consequence, the fracture surfaces are larger in the AUTODYN simulations.

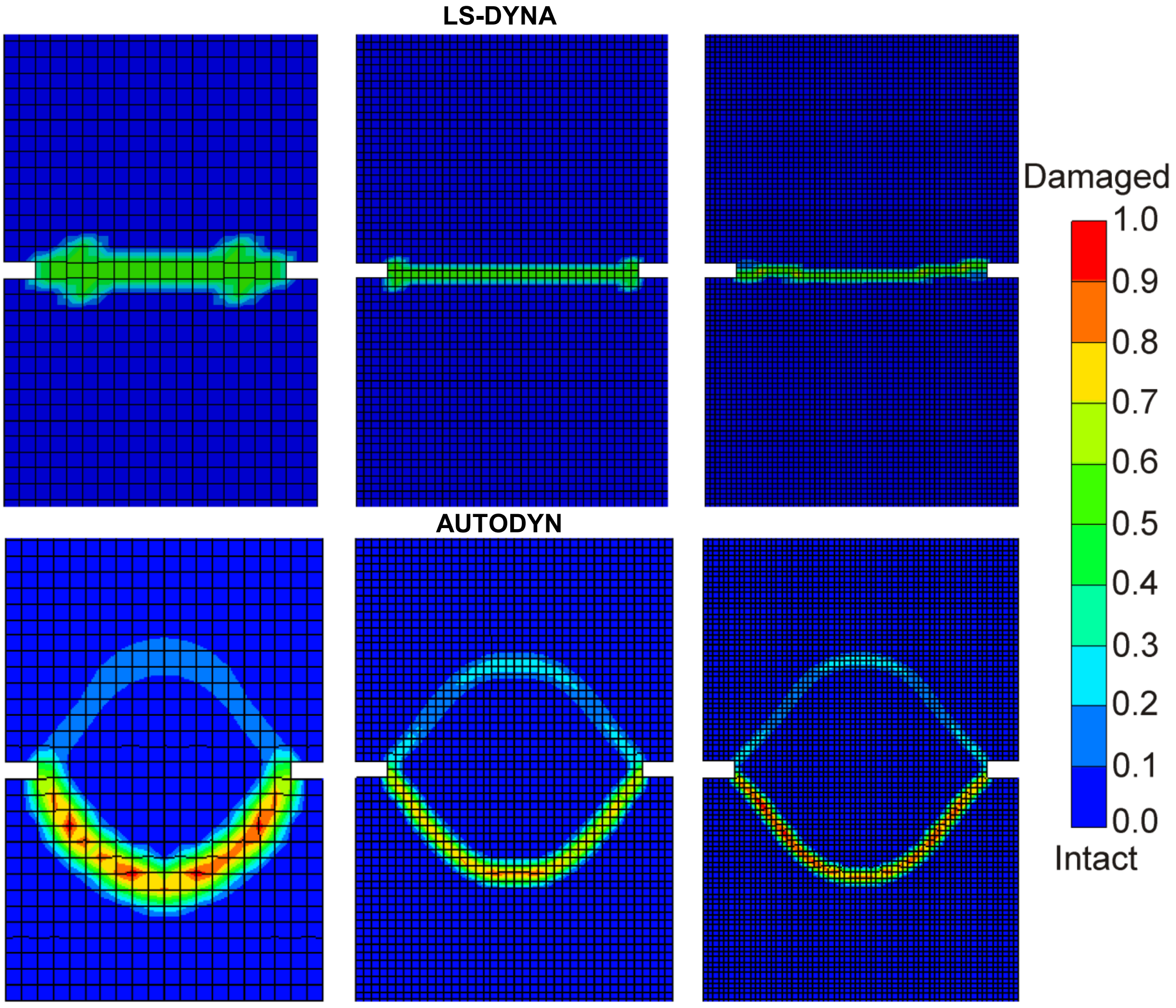

Coarse mesh size (3.0 mm) Middle mesh size (1.5 mm) Fine mesh size (1.0 mm)

Fig. 4: Code comparison of damage parameter contours in simulations with different mesh sizes of a tensile test with a notched specimen

Fig. 5 compares the tensile softening behaviour calculated with LS-DYNA and AUTODYN. As expected, both implementations are sensitive to mesh size. Finer meshes yield steeper softening slopes. Differences in maximum stresses can be attributed to differences of fracture surfaces.

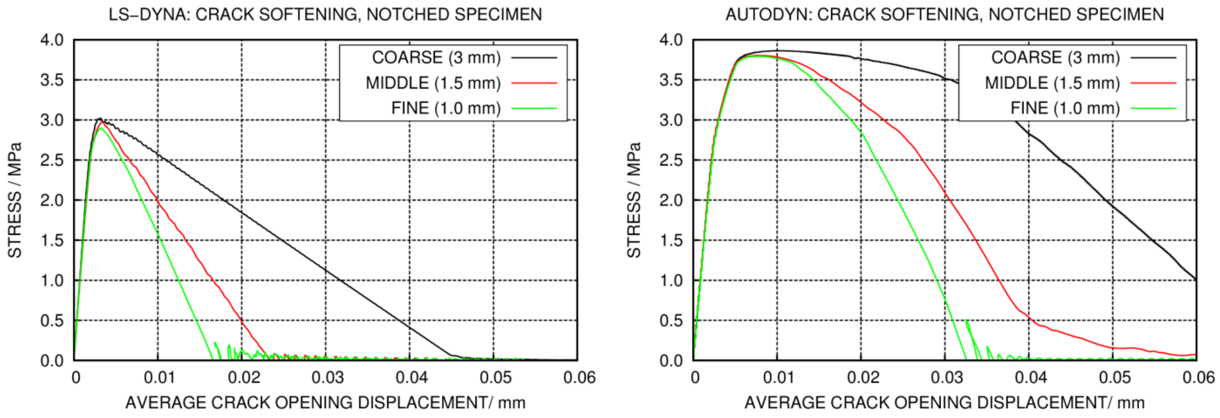

Fig. 5: Code comparison of tensile softening behaviour in simulations with different mesh sizes of a tensile test with a notched specimen

© 2017 Copyright by DYNAmore GmbH

4 Uniaxial and tri-axial compression

The failure surface of the RHT model is given by equation (16).

$$Y^*_{fail} = Y^*_{triax}(p)\cdot R_3(\vartheta)\cdot DIF\left(\dot{\varepsilon}\right) \tag{16}$$

The goal of this section is to consider quasi-static uniaxial and tri-axial material tests. The corresponding stress states are located on the compressive meridian with a Lode angle of $\vartheta = \pi/3$ that is $R_3 = 1$. Further, the dynamic increase factor is equal to unity in static tests. The compressive meridian is given by equation (17).

$$Y^*_{triax}\left(p^*\right) = \begin{cases} 0 \quad \text{if} \quad p^* \le HTL^* \\ -p^*\cdot f_s^*/\left(HTL^*\cdot Q_1\right) + f_s^*/Q_1 \quad \text{if} \quad HTL^* \le p^* \le 0 \\ 3\cdot p^*\cdot\left(1 - f_s^*/Q_1\right) + f_s^*/Q_1 \quad \text{if} \quad 0 < p^* < 1/3\cdot f_c^* \\ A_{fail} + B_{fail}\cdot\left(p^* - HTL^*\cdot DIF\right)^{n_{fail}} \quad \text{if} \quad 1/3\cdot f_c^* \le p^* \end{cases} \tag{17}$$

A_{fail} is derived by continuity conditions and therefore no input parameter. The hydrostatic tensile limit HTL^* can be calculated by equation (15). The parameters $Q_1 = R_3(\pi/6)$ and $Q_2 = R_3(0)$ are calculated from the Willam-Warnke form (see e. g. [4]), while tensile strength f_t^* and shear strength f_s^* are input parameters.

$$HTL^* = \frac{Q_2}{Q_1}\cdot\frac{f_t^*\cdot f_s^*}{3\cdot(f_t^* - f_s^*)} \tag{18}$$

The residual strength surface is given by equation (19). It does not depend on strain rate and Lode angle.

$$Y^*_{fric} = \begin{cases} 0 \quad \text{if} \quad p^* \le 0 \\ B_{fric}\cdot\left(p^*\right)^{n_{fric}} \quad \text{if} \quad p^* > 0 \end{cases} \tag{19}$$

A comparison of response to uniaxial compressive loading based on a single element simulation and the CONC-35 parameter set is presented in Fig. 6. In principle, the responses of the stress-strain-curves are assessed to be equivalent. However, some deviations in the softening branch and the damage evolution are visible. As expected, the response is elastic up to a stress of $comprat{*}f_c$. After this, hardening occurs until the compressive strength is reached. Then material damage is accumulated until the residual strength surface is reached. According to equation (19) the stress is not going to zero for totally crushed material at a finite hydrostatic pressure.

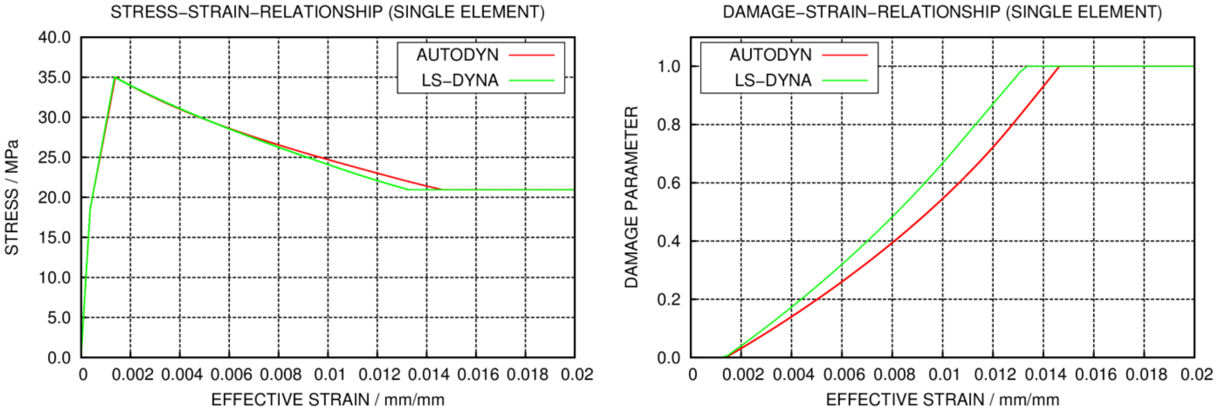

Fig. 6: Code comparison of uniaxial compression behaviour and damage parameter evolution in single-element simulations

In the frame of the activity IRIS data of unconfined and confined compressive tests were made available to the participants (see [7], [9]). In these tests with cylindrical specimens (see sketch in Fig. 8) the effective stress difference is given by the difference of applied pressure and confinement pressure according to equation (20).

$$\sigma_{eff} = \left|\sigma_{\max} - \sigma_c\right| \tag{20}$$

The maximum hydrostatic pressure can be derived from equation (21).

$$p = \frac{1}{3} \cdot \left(\sigma_{\max} + 2 \cdot \sigma_c\right) \tag{21}$$

Results of five material tests with different levels of confinement pressure are listed in Table 1. In this context the points (p,σ_{max}) are located on the compressive meridian of the failure surface.

σ_c	σ_{max}	p	σ_{eff}
0.0	69.1	23.0	69.1
15.5	128.1	53.0	112.6
26.0	166.1	72.7	140.1
47.0	233.7	109.2	186.7
100.0	392.4	197.5	292.4

Table 1 Results (in MPa) of compression tests provided in the frame of the activity IRIS [7], [9]

Fitting of compressive meridian model parameters to test data yielded B_{fail} = 1.82 and n_{fail} = 0.79. Regarding residual strength surface parameters, the pragmatic choices $B_{fric} = B_{fail}$ and $n_{fric} = n_{fail}$ were made. This is consistent with the CONC-35 parameter set. Fig. 7 compares fitted compressive meridians and residual strength surfaces with those of the CONC-35 parameter set. For larger confinement pressures the relative strength increase is larger for the fitted meridians. However, the relative residual strength is lower in the range of lower hydrostatic pressures.

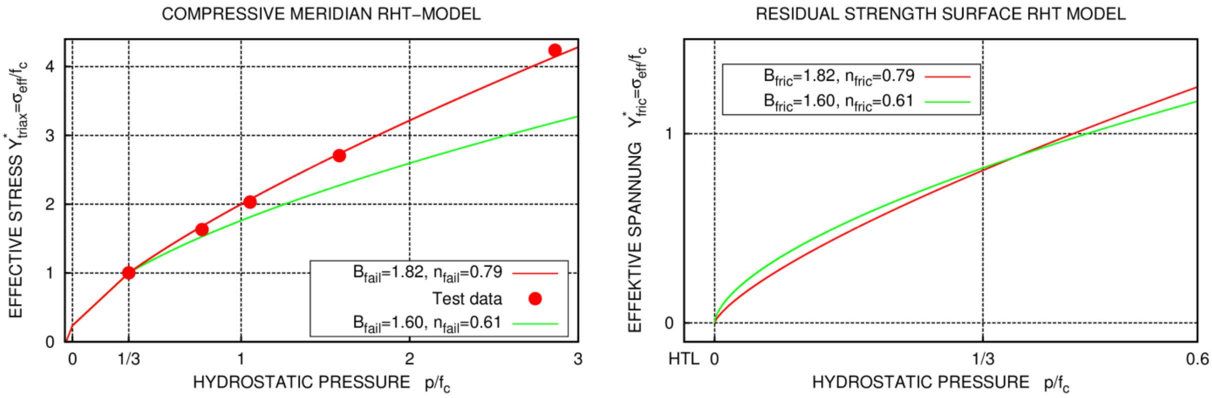

Fig. 7: Comparison of compressive meridians and residual strength surfaces for CONC-35 and fitted input parameter set

A comparison of measured and simulated stress-strain-relationships for different levels of confinement pressures is presented in Fig. 8. Despite differences regarding hardening in some cases the results are supposed to be equivalent. Obviously, the model is capable to consider also strain and related volume dilatation in the direction horizontally to the loading. Future work should include simulations dealing with a finer discretization of the test specimens to figure out structural effects and representation of crack patterns.

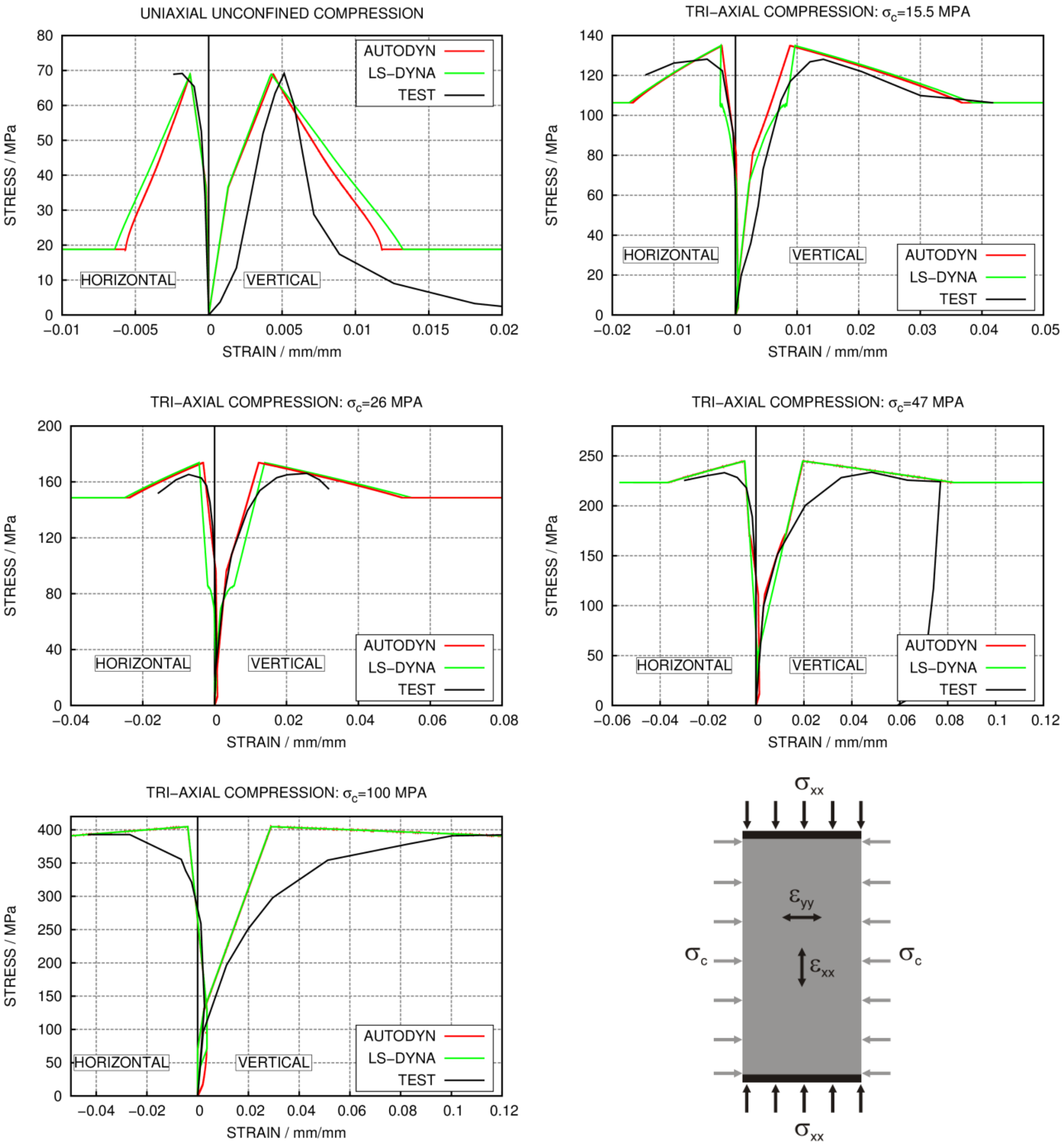

Fig. 8: Code comparison of stress strain relationships for different confinement pressures

5 Simulation of hard missile impact tests

A code comparison regarding the application of the RHT concrete model is presented on the basis of simulations of a series of hard missile impact tests carried out at VTT. These tests are dealing with punching and perforation failure of 250 mm thick reinforced concrete slabs impacted at different velocities by pipes with domed shaped noses and a light weight concrete filling. The missile design corresponds to a total mass of about 47 kg. Details of the experimental setup are given in [13]. The tests P1 – P3 carried out in the frame of the activity IRIS belong to this test matrix. Numerical studies on IRIS punching tests were presented in previous LS-DYNA conferences by Van Dorsselaer et al. [14], [15], [16]. The IRIS test was repeated three times with impact velocities of about 135 m/s. Fig. 9 shows some basic dimensions of a simulation model with an average element size of 10 mm. In the frame of this paper slabs without shear reinforcement are considered, only. Bending reinforcement is incorporated by bars (Ø = 10 mm) with a spacing of 90 mm each way and each face. The coupling of

© 2017 Copyright by DYNAmore GmbH

reinforcement and concrete is achieved by the shared nodes approach. Horizontal and vertical bending reinforcement layers are separated by one layer of solid concrete elements. In the test the slab edges are covered by steel sheets of 100 mm width, which are included in the model by shell elements. The two-way support boundary condition is considered by nodal displacement constraints in the direction of impact along each edge.

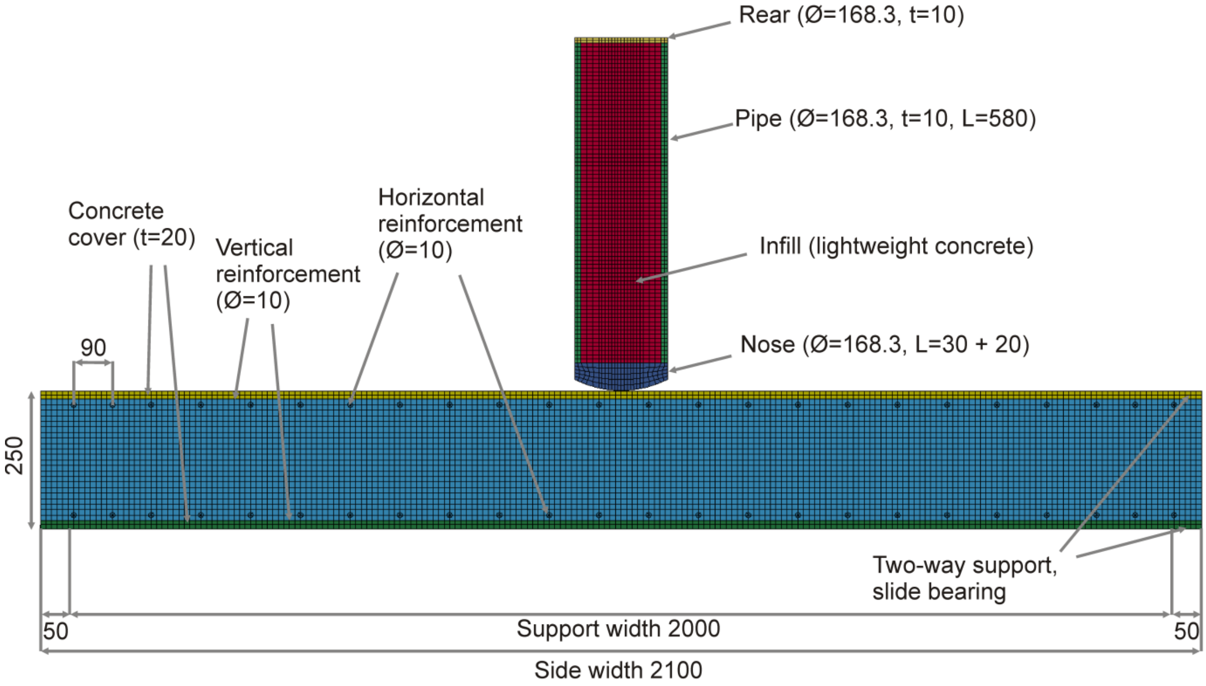

Fig. 9: Model setup for VTT punching test simulations (measurements in mm)

Fig. 10 compares contours of the concrete damage parameter distributions on the back face of the slab after the test with the damage status of the selected test P1. The slab was perforated by the missile, which is obviously reproduced by the simulations. Since the horizontal reinforcement bars are located close to the surface, the extent of scabbed area is larger in horizontal direction. Thanks to the separation of vertical and horizontal reinforcement in the numerical mesh, both simulations are capable to reproduce this asymmetry.

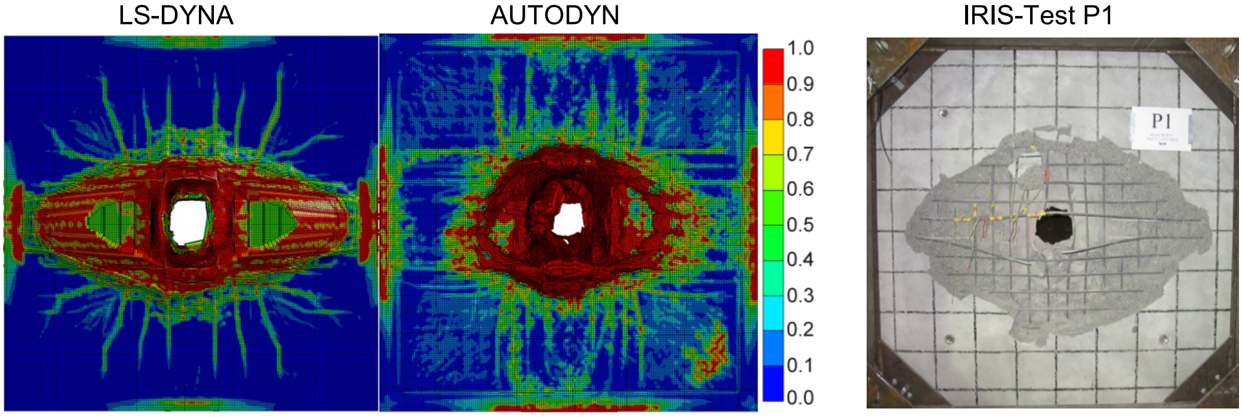
LS-DYNA AUTODYN IRIS-Test P1

Fig. 10: Code comparison of damage parameter contours on the back face of the slab

Fig. 11 compares damage parameter distributions in horizontal and vertical slab sections with sections of a selected test slab. The process of perforation of concrete slabs by rigid missiles may be described as a sequence of initial cratering phase, tunnelling phase and a shearing out phase [17]. Apparently, both simulations as well as the test result indicate the formation of a shear cone. Some differences regarding shear cone angle and extent of scabbed area are visible among the simulation results.

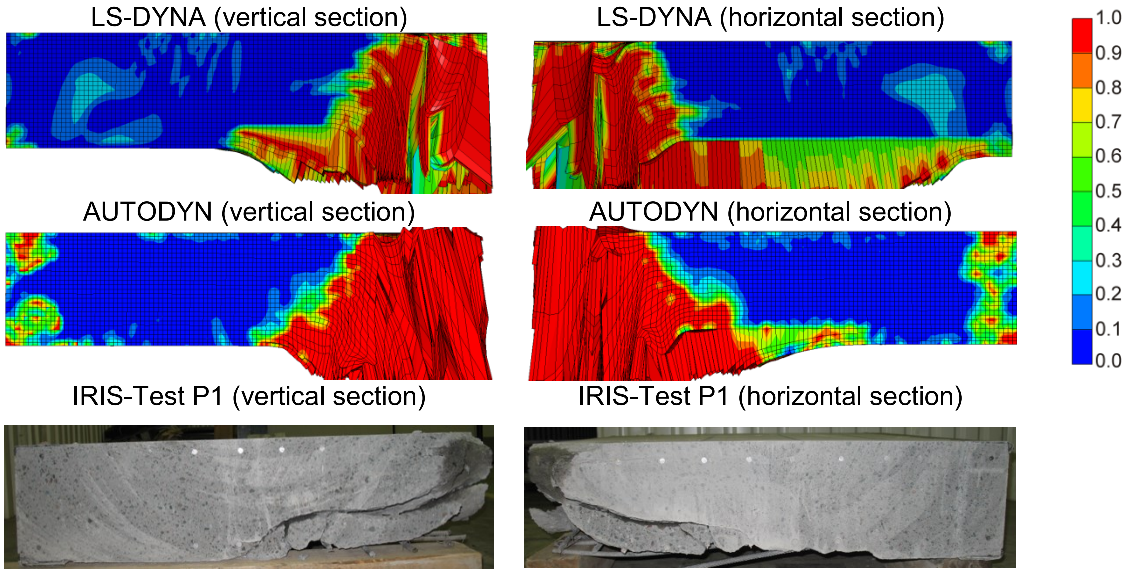

Fig. 11: Code comparison of damage parameter contours in horizontal and vertical slab sections

Fig. 12 (left part) compares results regarding calculated velocity-time histories of the rear of the missile. It should be emphasized that in the simulations the residual strength surface based on compressive tests was used (see Fig. 7, left part). During the initial phase quite identical results are observed and both simulations yield a residual exit velocity in the range of experimental scattering. However, some differences appear in the shearing out phase. Results of a parametric study regarding impact velocity are shown in Fig. 12 (right part). By trend, the AUTODYN simulations indicate larger residual velocities and a lower ballistic limit than the LS-DYNA simulations. Besides the IRIS data also results from other punching tests are included. It has to be mentioned that some scattering regarding material properties exists among the different slabs, while the numerical parametric study was performed with a fixed set of material input parameter.

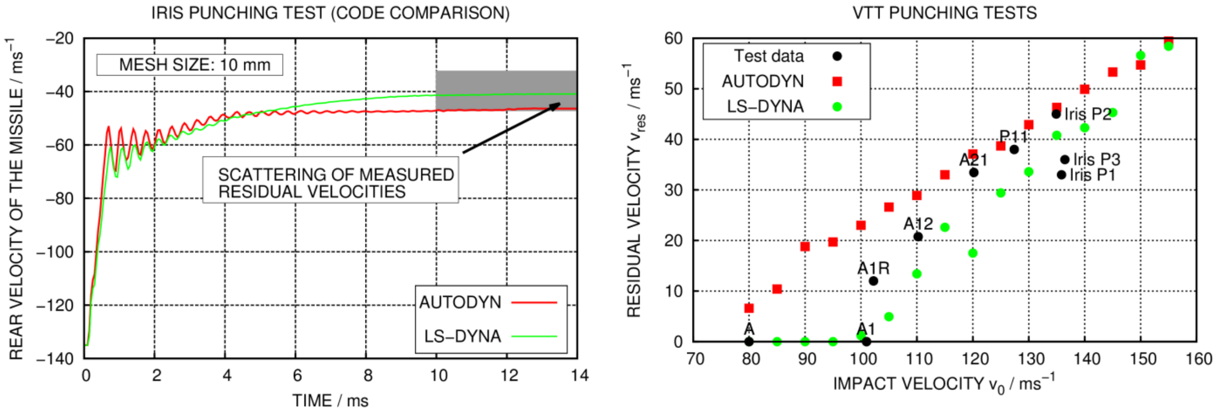

Fig. 12: Code comparison for residual missile velocities for a mesh size of 10 mm

Another parametric study is dealing with the effect of mesh size. Fig. 13 shows results of simulations with an average mesh size of 7.5 mm. It is apparent from the results that there is a substantial influence of mesh size on residual missile velocity, which seems to emerge in the beginning of the shearing out phase. In principle the shearing out process is assumed to take place at low hydrostatic pressures and shear stresses. Therefore, the dependency on mesh size is consistent with the conclusions of section 3 of this paper.

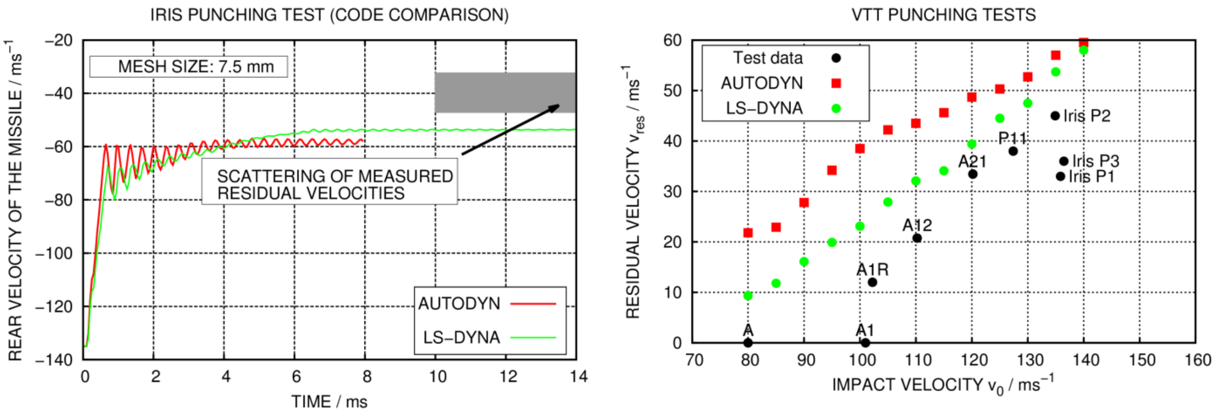

Fig. 13: Code comparison for residual missile velocities for an average mesh size of 7.5 mm

In addition, results from simulations with CONC-35 default parameters for failure surface and residual strength surface shape are presented in Fig. 14. The influence of these parameters on residual velocity is highly pronounced. Astonishingly, the residual velocities are much lower in this study, especially for the LS-DYNA simulations. This may be attributed to the shape of the residual strength surface at low hydrostatic pressures (compare Fig. 7, left part). It is mentioned in [14] that the residual missile velocity is highly sensitive to the residual strength surface parameter *a1f* of the Karagozian&Case model **`*MAT_CONCRETE_DAMAGE_REL3`**. In principle the results shown in Fig. 14 may confirm this finding. Further, there is a substantial influence on the ballistic limit velocity. Other relevant parameters regarding residual velocity seem to be material properties, especially failure criteria, for reinforcement steel (see [10]).

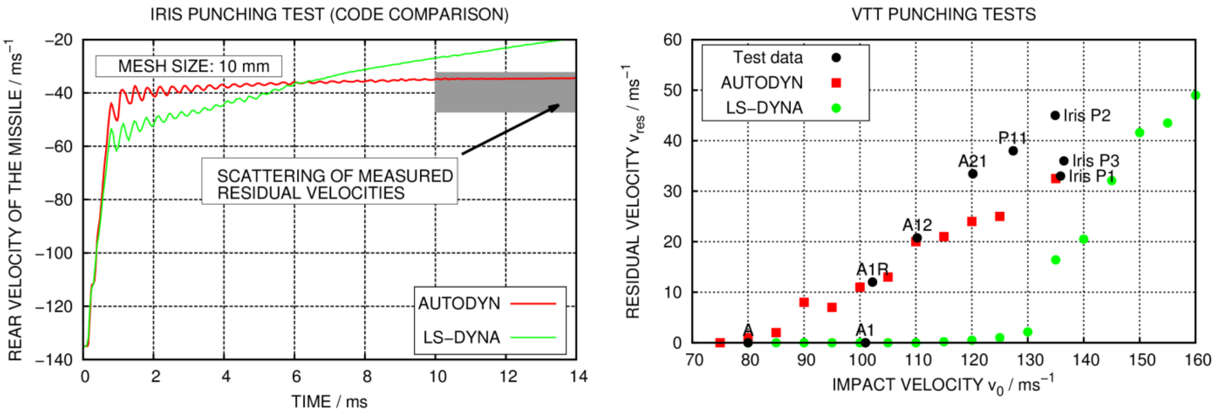

Fig. 14: Code comparison for residual missile velocities for CONC-35 strength surface and residual surface parameter (B_{fail} = B_{fric} = 1.6, n_{fail} = n_{fric} = 0.61)

The results presented in this section show that in principle the perforation of a reinforced concrete slab can be simulated with LS-DYNA and AUTODYN using the RHT concrete model. It seems to be mandatory to perform parametric studies, since the results depend on modelling parameters. In general it is advised to consider a certain range of impact velocities. Furthermore, it would be beneficial to study variations of the thickness of the slab as well as reinforcement layout.

6 Summary and conclusion

This paper presents a comparison of the RHT concrete material model implementations in the analysis codes ANSYS AUTODYN and LS-DYNA. The quasi-static behaviour is compared for different stress conditions. Further results of validation studies on the simulation of selected hard missile impact tests with reinforced concrete slabs are presented.

Regarding hydrostatic compression the LS-DYNA implementation deviates from the AUTODYN simulation. In this context the AUTODYN implementation is assumed to cover the theoretical background of the employed equations correctly.

AUTODYN simulation results of tensile tests with notched specimens are unrealistic with cracks located outside the planes of the notches, while the crack distributions calculated with LS-DYNA are supposed to be more realistic in these cases.

Concerning uniaxial compression and confined tri-axial compression results from both implementations are assessed to be equivalent.

A comparative validation study based on impact tests dealing with punching and perforation failure of reinforced concrete slabs subjected to hard missile impact is presented. Results regarding residual exit velocities of the missile depend among other parameters on mesh size. This is attributed to the shearing out process which is supposed to occur at relatively low hydrostatic stresses close to the tensile limit of failure surface and residual strength surface.

Therefore the most important result is that in general the failure model implementations do not consider discretisation length or fracture energy. Consequently simulation results are sensitive to the mesh size, i.e. presently application cases in the frame of safety assessments need adequate test results. In this context the authors recommend to improve the concrete failure model concerning the sensitivity on mesh size.

7 Annex: Input parameter sets

This section provides input parameter sets used in the simulations. The parameters are listed separately regarding EOS (Table 2), strength model (Table 3) and damage model (Table 4). For quasi-static simulations the compressive and tensile strain rate parameters α_{sr} and δ_{sr} were set to zero. As mentioned in this paper, a parameter for bulk modulus or porous sound-speed of concrete is missing in the LS-DYNA implementation. Further, some parameters regarding internal energy (T_{ref}, C_v, k) are missing. Concerning the damage model no parameter corresponding to the residual shear modulus G_{res} of totally destroyed concrete could be identified. The LS-DYNA implementation requires to enter the parameters E0C (default 3E-5/s) and E0T (default 3E-6/s) for reference compressive and tensile strain rates. In the AUTODYN implementation these values are hardwired. Break compressive strain rate EC as well as break compressive strain rate ET are missing in the AUTODYN implementation. According to [4] a very large value is chosen here. Finally, the LS-DYNA implementation provides the parameter PTF describing the direction of plastic flow in tension, which is missing in AUTODYN (see section 3).

Concrete EOS: p-α EOS input parameters					
Variable	**Meaning**	**Unit**	**Conc-35** [1]	**Fitted to IRIS-Tests** [9]	**Related parameter in LS-DYNA** [4]
$\rho_{solid,0}$	Reference density	g/cm^3	2.75	2.75	RO*ALPHA
ρ_{porous}	Porous density	g/cm^3	2.314	2.298	RO
c_e	Porous sound-speed	m/s	2.92E+3	2.25E+3	Missing
p_{el}	Initial compaction pressure	kPa	2.33E+4	4.61E+4	PEL
p_s	Solid compaction pressure	KPa	6.00E+6	6.00E+6	PCO
n	Compaction exponent	-	3.0	3.0	NP
Solid EOS	Type of Solid EOS	-	Polynomial	Polynomial	No options available
A_1	Bulk modulus matrix	kPa	3.527E+7	3.527E+7	A1
A_2	Parameter A_2	kPa	3.958E+7	3.958E+7	A2
A_3	Parameter A_3	kPa	9.04E+6	9.04E+6	A3
B_0	Parameter B_0	-	1.22	1.22	B0
B_1	Parameter B_1	-	1.22	1.22	B1
T_1	Parameter T_1	kPa	3.527E+7	3.527E+7	T1
T_2	Parameter T_2	kPa	0.0	0.0	T2
T_{ref}	Reference temperature	K	300	200	Missing
C_v	Specific heat	J/kgK	6.54E+02	6.54E+02	Missing
k	Thermal conductivity	W/mK	0.0	0.0	Missing
Curve	Type of compaction curve	-	alpha plastic	alpha plastic	No options available

Table 2: EOS parameter (unit system mm, mg, ms)

Concrete strength model: RHT strength model input parameters					
Variable	**Meaning**	**Unit**	**Conc-35** [1]	**Fitted to IRIS-Tests** [9]	**Related parameter in LS-DYNA** [4]
G	Shear modulus	GPa	16.7	11.7	SHEAR
f_c	Compressive strength	MPa	35.0	69.1	FC
f_t/f_c	Tensile strength	-	0.10	0.06	FT*
f_s/f_c	Shear strength	-	0.18	0.18	FS*
B_{fail}	Intact Failure Surface Constant	-	1.6	1.82	A
n_{fail}	Intact Failure Surface Constant	-	0.61	0.79	N
$Q_{2,0}$	Tens./Comp. Meridian	-	0.6805	0.6805	Q0
BQ	Brittle to ductile transition	-	1.05E-02	1.05E-02	B
ratio	G(elas)/(elas.-plas.)	-	2.0	2.0	1/XI
tensrat	Elastic strength / f_t	-	0.7	0.7	GT*
comprat	Elastic strength / f_c	-	0.53	0.53	GC*
B_{fric}	Fracture strength constant	-	1.6	1.82	AF
n_{fric}	Fracture strength exponent	-	0.6	0.79	NF
α_{sr}	Compressive strain rate exp.	-	3.2E-2	1.76E-2	BETAC
δ_{sr}	Tensile strain rate exp.	-	3.6E-2	2.24E-2	BETAT
CAP	Use CAP on elastic surface?	-	Yes	Yes	No options available

Table 3: Strength model parameter (unit system mm, mg, ms)

Concrete failure model: RHT failure model input parameters					
Variable	**Meaning**	**Unit**	**Conc-35** [1]	**Fitted to IRIS-Tests** [9]	**Related parameter LS-DYNA** [4]
D_1	Damage constant	-	0.04	0.04	D1
D_2	Damage exponent	-	1.0	1.0	D2
$\varepsilon_{f,min}$	Minimum strain to failure	-	0.01	0.01	EPM
Tensile failure	Tensile failure criteria	-	Hydro. p_{min}	Hydro. p_{min}	No options available
G_{res}	Residual / elastic Shear Modulus	-	0.13	0.13	Missing
Erosion	Erosion strain	%	200	200	EPSF

Table 4: Failure model parameter (unit system mm, mg, ms)

8 Literature

[1] Riedel, W.: "Beton unter dynamischen Lasten. Meso- und makromechanische Modelle und ihre Parameter", Fraunhofer IRB Verlag, 2004

[2] Riedel, W. et al.: "Numerical assessment for impact strength measurements in concrete materials", International Journal of Impact Engineering, Volume 36, Issue 2, 2009, 283-293

[3] ANSYS Inc.: "ANSYS® AUTODYN® x64", Release 16.1, 2016

[4] Borrvall, T., Riedel, W.: "The RHT Concrete Model in LS-DYNA", 8th European LS-DYNA Users Conference, Strasbourg, 2011

[5] Livermore Software Technology Corporation (LSTC): "LS-DYNA® Keyword User's Manual, Volume I and II", Version LS-DYNA R8.0 03/23/15(r:6319), 2015

[6] Herrmann, W.:" Constitutive Equation for the Dynamic Compaction of Ductile Porous Materials", Journal of Applied Physics, Volume 40, Number 6, 1969, 2490-2499

[7] Orbovic, N.: " IRIS2012 OECD/NEA/CSNI benchmark: Numerical simulations of structural impact", Nuclear Engineering and Design, Volume 295, 2015, 700-715

[8] Nuclear Energy Agency (NEA): "Improving Robustness Assessment Methodologies for Structures Impacted by Missiles (IRIS_2010)", Final Report NEA/CSNI/R(2011)8, 2012

[9] Nuclear Energy Agency (NEA): "Improving Robustness Assessment Methodologies for Structures Impacted by Missiles (IRIS_2012)", Final Report NEA/CSNI/R(2014)5, 2014

[10] Gesellschaft für Anlagen- und Reaktorsicherheit (GRS) gGmbH: "Weiterentwicklung der Analysemethodik zur Berücksichtigung komplexer Lastannahmen bei hochdynamischen Einwirkungen auf Stahlbetonstrukturen", GRS – 410, ISBN 978-3-944161-92-1, 2016

[11] Carrol, M. M., Holt, A. C.: "Dynamic and static Pore-Collapse Relations for Ductile Porous Materials", Journal of Applied Physics, Volume 43, 1972, 1626-1636

[12] Leppänen, J: "Concrete subjected to projectile and fragment impacts: Modelling of crack softening and strain rate dependency in tension", International Journal of Impact Engineering, Volume 32, 2006, 1828-1841

[13] Heckötter, C., Vepsä, A.: "Experimental investigation and numerical analyses of reinforced concrete structures subjected to external missile impact", Progress in Nuclear Energy, Volume 84, 2015, 56-67

[14] Van Dorsselaer, N. et al.: "Impact Simulations on Concrete Slabs: LS-OPT® Fitting Approach", 8th European LS-DYNA Users Conference, Strasbourg, 2011

[15] Van Dorsselaer, N. et al.: "General Approach for Concrete Modeling: Impact on Reinforced Concrete", 12th International LS-DYNA® Users Conference, Dearborn, 2012

[16] Van Dorsselaer, N. et al.: "LS-OPT Parameter Identification on Concrete Sample Tests for an Impact Simulation on Concrete Slab", 9th European LS-DYNA Conference, Manchester, 2013

[17] Li, Q.M. et al.: "Local impact effects of hard missiles on concrete targets", International Journal of Impact Engineering, Volume 32, 2005, 224-284